1 E06-014

A Precision Measurement of d_2^n: Probing the Lorentz Color Force

S. Choi, X. Jiang, Z.-E. Meziani, B. Sawatzky, spokespersons,
and
the d_2^n and Hall A Collaborations.
Contributed by D. Flay.

1.1 Physics Motivation

1.1.1 d_2^n: Quark-Gluon Correlations in the Nucleon

To date, extensive work has been done investigating the spin structure function g_1 within the context of the Feynman parton model and pQCD. However, far less is known about the g_2 structure function. It is known to contain quark-gluon correlations. It follows from a spin-flip Compton amplitude and may be written as:

$$g_2\left(x,Q^2\right) = g_2^{WW}\left(x,Q^2\right) + \bar{g}_2\left(x,Q^2\right), \tag{1}$$

where g_2^{WW} is the Wandzura-Wilczek term, which may be expressed entirely in terms of g_1 [1]:

$$g_2^{WW}\left(x,Q^2\right) = -g_1\left(x,Q^2\right) + \int_x^1 \frac{g_1\left(y,Q^2\right)}{y} dy. \tag{2}$$

The second term is given as:

$$\bar{g}_2\left(x,Q^2\right) = -\int_x^1 \frac{1}{y}\frac{\partial}{\partial y}\left[\frac{m_q}{M} h_T\left(y,Q^2\right) + \xi\left(y,Q^2\right)\right] dy, \tag{3}$$

where h_T is the transverse polarization density, and ξ is a term arising from quark-gluon correlations. Here, h_T is suppressed by the ratio of the quark mass m_q to the target mass M. Therefore, a measurement of $\bar{g}_2$ provides access to quark-gluon interactions inside the nucleon [2].

Additionally, a measurement of both g_1 and g_2 allows for the determination of the quantity d_2^n, which is formed as the second moment of a linear combination of g_1 and g_2:

$$d_2^n\left(Q^2\right) = \int_0^1 x^2\left[2g_1^n\left(x,Q^2\right) + 3g_2^n\left(x,Q^2\right)\right] dx = 3\int_0^1 x^2 \bar{g}_2^n\left(x,Q^2\right) dx. \tag{4}$$

d_2^n also appears as a matrix element of a twist-3 operator in the operator product expansion [3]:

$$\langle P,S \mid \bar{\psi}_q(0)\, gG^{+y}(0)\gamma^+ \psi_q(0) \mid P,S\rangle = 2MP^+P^+S^x d_2^n, \tag{5}$$

where $G^{+y} = \frac{1}{\sqrt{2}}\left(B^x - E^y\right)$. We see from Equations 3–5 that d_2^n is a twist-3 matrix element that measures quark-gluon interactions.

Recent work has shown [4, 5] that at high Q^2, d_2^n is seen as a color Lorentz force averaged over the volume of the nucleon. This is given by the expression of the transverse (color) force on the active quark immediately following its interaction with a virtual photon:

$$F^y(0) \equiv -\frac{\sqrt{2}}{2P^+}\langle P,S \mid \bar{\psi}_q(0)\, gG^{+y}(0)\gamma^+ \psi_q(0) \mid P,S\rangle = -\frac{1}{2}M^2 d_2^n. \tag{6}$$

This theoretical interpretation reveals how g_2 and subsequently d_2^n will allow us to examine the color interactions of the constituents inside the nucleon.

While bag and soliton model calculations of d_2 for the neutron yield numerical values consistent with those of lattice QCD, current experimental data differs by roughly two standard deviations (see the highest Q^2 data in Figure 1). One of the goals of our experiment is to improve the experimental error on the value of d_2^n by a factor of four. It subsequently provides a benchmark test of lattice QCD calculations, shown in Figure 1.

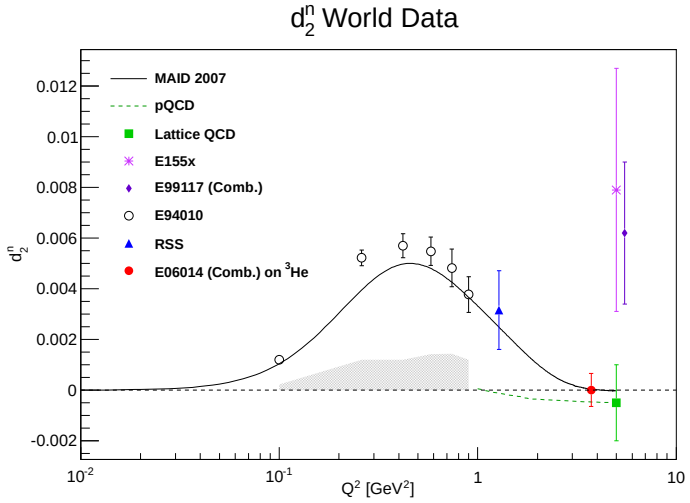

Figure 1: d_2^n as a function of Q^2. All the data shown with the exception of the SLAC E155x data are dominated by resonance contributions. E06-014 data will observe mostly the deep inelastic scattering (DIS) contribution. The projected error on from E06-014 [6] is shown, along with the lattice QCD result [7]. The dashed green curve shows the pQCD evolution from the lattice point [8] based on the calculations of [9, 10]. Data from JLab experiments E94-010 [11, 12] and RSS [13] are included in the plot. For comparison to the resonance contribution, a MAID model [14] is plotted. Also plotted is the total d_2 from SLAC experiment E155x [15].

1.1.2 A_1: The Virtual Photon-Nucleon Asymmetry

Another quantity of interest is the virtual photon-nucleon longitudinal spin asymmetry A_1. It provides insight into the quark structure of the nucleon and can be defined as:

$$A_1\left(x,Q^2\right) \equiv \frac{\sigma_{1/2}-\sigma_{3/2}}{\sigma_{1/2}+\sigma_{3/2}}, \tag{7}$$

where the subscript 1/2 (3/2) gives the projection of the total spin of the virtual photon-nucleon system along the virtual photon direction corresponding to the nucleon's spin anti-parallel (parallel) to the virtual photon. Constituent quark models (CQM) and pQCD models predict A_1 to be large and positive at large x. Figure 2(a) shows the current world data compared to these models. It is seen that the CQM (yellow band [16]) describes the trend of the data reasonbly well. The pQCD parameterization with hadron helicity conservation (dark blue curve [21])—assuming quark orbital angular momentum to be zero—does not describe the data well. However, the pQCD model allowing for quark orbital angular momentum to be non-zero (green curve [23]) describes the data well, pointing perhaps to the importance of quark orbital angular momentum in the spin structure of the nucleon.

Combining A_1^n data measured on a polarized effective neutron target with A_1^p data measured on a polarized proton target allows access to $\Delta u/u$ and $\Delta d/d$. Recent results from Hall A [20] and from CLAS [24] showed a significant deviation of $\Delta d/d$ from the pQCD predictions, which have that ratio approaching 1 in the limit of $x \to 1$ (Fig. 2(b)). As part of the 12 GeV program, two approved experiments (one in Hall A [25] and one in Hall C [26]) will extend the accuracy and x range of this measurement, but a measurement of A_1^n at the kinematics of this experiment (E06-014) will provide valuable support (or refutation) of prior JLab results, while producing additional input for theoretical models in advance of the coming experiments at 12 GeV.

1.2 The Experiment

The experiment ran in Hall A of Jefferson Lab from February to March of 2009, with two beam energies of $E = 4.74$ and 5.89 GeV, covering the resonance and deep inelastic valence quark regions, characterized by $0.2 \leq x \leq 0.7$ and $2\ \text{GeV}^2 \leq Q^2 \leq 6\ \text{GeV}^2$. The coverage in the x and Q^2 plane is shown in Figure 3.

In order to measure d_2^n, we scattered a longitudinally polarized electron beam off of a ^{3}He target, in two polarization configurations – longitudinal and transverse. ^{3}He serves as an effective polarized neutron target since roughly 86% of

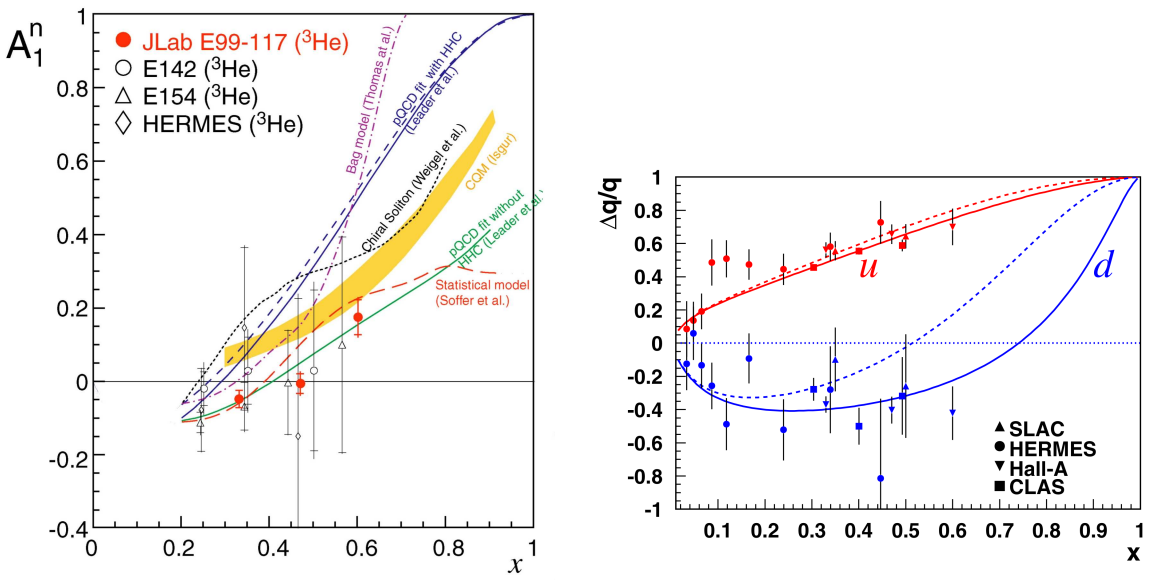

(a) A_1^n

(b) $\Delta d/d$ and $\Delta u/u$

Figure 2: Current data for A_1^n, $\Delta d/d$ and $\Delta u/u$. (a): The current world data for the neutron A_1 from SLAC E143 [17] and E154 [18] and HERMES [19], along with JLab E99-117 [20]. Also shown are CQM models and various pQCD models; (b): $\Delta q/q$ for the up (u) and down (d) quarks. The dashed curves represent a prediciton from Leader *et al.* [21], while the solid curves show calculations by Avakian *et al.* [22]. The data shown is from HERMES, SLAC and JLab.

the polarization is carried by the neutron. This is due to the two protons in the nucleus being primarily bound in a spin singlet state [27, 28].

We measured the unpolarized cross section σ_0 and the double-spin asymmetries $A_\parallel$ and $A_\perp$. The cross section was measured by the Left High-Resolution Spectrometer (LHRS), while the asymmetries were measured by the BigBite Spectrometer. The LHRS and BigBite were oriented at scattering angles of $\theta = 45^\circ$ to the left and right of the beamline, respectively.

Expressing the structure functions entirely in terms of these experimental quantities, we have the expression for d_2:

$$d_2 = \int_0^1 \frac{MQ^2}{4\alpha^2}\frac{x^2y^2}{(1-y)(2-y)}\sigma_0\left[\left(3\frac{1+(1-y)\cos\theta}{(1-y)\sin\theta}+\frac{4}{y}\tan(\theta/2)\right)A_\perp+\left(\frac{4}{y}-3\right)A_\parallel\right]dx, \tag{8}$$

where $x = Q^2/2M\nu$, $\nu = E - E'$ is the energy transfer to the target, E' is the scattered electron energy, and $y = \nu/E$ is the fractional energy transfer to the target. The asymmetries are given by:

$$A_\parallel = \frac{N^{\downarrow\Uparrow} - N^{\uparrow\Uparrow}}{N^{\downarrow\Uparrow} + N^{\uparrow\Uparrow}} \quad \text{and} \quad A_\perp = \frac{N^{\downarrow\Rightarrow} - N^{\uparrow\Rightarrow}}{N^{\downarrow\Rightarrow} + N^{\uparrow\Rightarrow}},$$

where N is the number of electron counts measured for a given configuration of beam helicity (single arrows) and target spin direction (double-arrows).

While d_2 was the main focus of the experiment, the measurement of the asymmetries allowed for the extraction of A_1, according to:

$$A_1 = \frac{1}{D(1+\eta\xi)}A_\parallel - \frac{\eta}{d(1+\eta\xi)}A_\perp, \tag{9}$$

where D, η, ξ and d are kinematic factors [29].

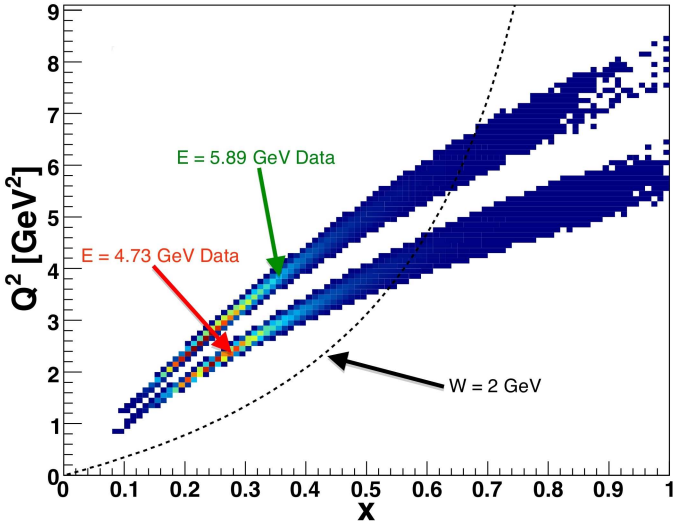

Figure 3: The E06-014 kinematic coverage in Q^2 and x. The lower band is the 4.74 GeV data set and the upper band is the 5.89 GeV data set. The black dashed line shows W = 2 GeV. The data to the left and right of this line corresponds to DIS and resonance data, respectively.

1.3 Data Analysis Progress

1.3.1 Summary of Completed Work

A number of analyses for E06-014 have been completed, including detector calibrations for both the LHRS and the BigBite spectrometer [33] and various background studies for the spectrometers corresponding to nitrogen dilution in the target and pair-produced electrons [34, 35].

The experiment used a polarized electron beam at energies of 4.74 and 5.89 GeV. The polarization of the electron beam was measured independently through Compton and Møller scattering, and the analysis of these measurments revealed a beam polarization of $\sim 72\%$ [35].

Knowledge of the target polarization is crucial when performing a double-spin asymmetry experiment. E06-014 used the standard Hall A polarized ^{3}He target with two holding field directions: longitudinal and transverse in plane, with respect to the electron beam direction. The target polarization was extracted through electron paramagnetic resonance (EPR). The longitudinal polarization was cross checked using nuclear magnetic resonance (NMR) measurements. During the running of the experiment, the polarization of the target was $\sim 50\%$ [35].

1.3.2 Unpolarized Cross Sections

The LHRS was used to measure the unpolarized cross section. The analysis for the extraction of the experimental cross section, σ_{rad}, for the E = 4.74 GeV and 5.89 GeV data sets is shown in [34].

1.3.3 Unpolarized Cross Section Radiative Corrections

Electrons lose energy due to interactions with material. This includes the material before and after the target, and the target material itself. These interactions will alter the electron's *true* incident energy and also its *true* scattered energy. This ultimately results in a different cross section than the true value. These effects are characterized by ionization (or Landau straggling) and bremmstrahlung. There are also higher-order processes at the interaction vertex that must also be considered. Collectively, the removal of these effects is called *radiative corrections*.

A first correction that must be done *before* carrying out the radiative corrections is to subtract the elastic radiative tail, since it is long and affects all states of higher invariant mass W [36]. For these kinematics, the elastic tail is small

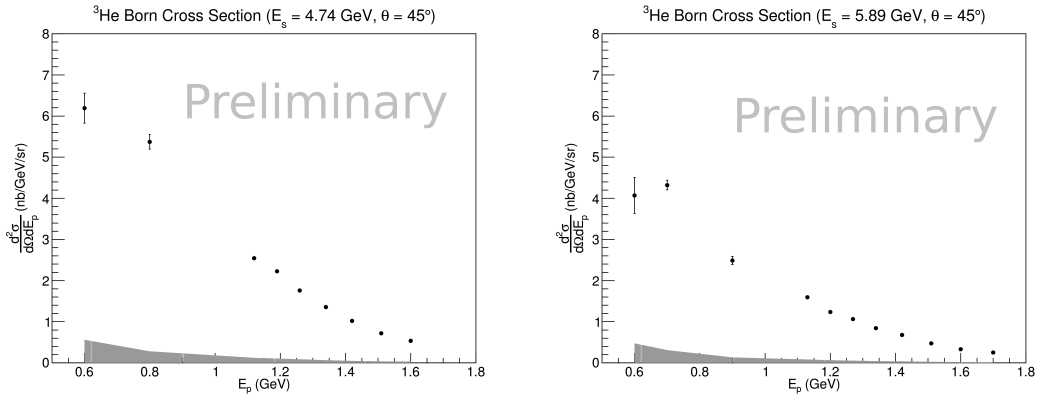

(a) E_s = 4.74 GeV (b) E_s = 5.89 GeV

Figure 4: The ^{3}He Born cross sections. The error bars indicate the statistical error, while the band indicates the systematic error. (a): E_s = 4.74 GeV data; (b): E_s = 5.89 GeV data.

and affects the lowest bins in scattered electron energy E_p at the $\lesssim 1\%$ level. The elastic tail was computed using the ROSETAIL code [37]. The model used for the elastic ^{3}He form factors were those from Amroun [38].

The ^{3}He quasi-elastic tail, however, is much larger. The quasi-elastic radiative tail was computed by utilizing an appropriate model of the ^{3}He quasi-elastic cross section [39] and applying radiative effects to it [40]. The tail was then subtracted from the data. The model was checked against existing quasi-elastic ^{3}He data covering a broad range of kinematics.

In considering the effects mentioned above, the *measured* cross section is realized in terms of a triple-integral:

$$\sigma_{\rm rad}\left(E_s,E_p\right) = \int_0^T \frac{dt}{T} \int_{E_s^{min}}^{E_s} dE_s' \int_{E_p}^{E_p^{max}} dE_p' I\left(E_s,E_s',t\right) \sigma_r\left(E_s',E_p'\right) I\left(E_p,E_p',T-t\right), \tag{10}$$

where $\sigma_{\rm rad}$ is the measured (radiated) cross section, σ_r is the *internally*-radiated cross section. E_s is the incident electron energy, E_p is the scattered electron energy. $I\left(E_0,E,t\right)$ is the probability of finding an electron with incident energy E_0 that has undergone bremmstrahlung with energy E at a depth t inside a material [36, 40].

In order to *unfold* the Born cross section, an iterative procedure is carried out in RADCOR [41]. It amounts to calculating:

$$\sigma_b^i = \frac{1}{\rm C}\left[\sigma_{\rm rad} - \int(\ldots)\,dE_s' - \int(\ldots)\,dE_p'\right], \tag{11}$$

where C and the two integrals are defined in Equation IV.2 in [36]. σ_b^i is the Born cross section obtained for the $i^{\rm th}$ iteration of the code, $\sigma_{\rm rad}$ is the radiated cross section to be corrected. σ_b^i is then re-inserted into equation for the next iteration. It was found that the calculation converges within the first 3–4 iterations. Figure 4 shows the Born cross sections.

In E06-014, we took data for only two E_s values of 4.74 GeV and 5.89 GeV. However, we need enough data to properly calculate the integrals above. Therefore, we used a suitable cross section model [42] to fill in the rest of the phase space for each data set.

1.3.4 Unpolarized Cross Section Systematic Errors

There are a number of contributions to the systematic errors on the cross section calculation [35]. We will focus our discussion on the radiative corrections.

The systematic errors corresponding to the radiative corrections include the elastic and quasi-elastic tail subtraction, material thicknesses in the electron's path, and dependence on the input model used for the radiative correction calculations.

The systematic error of subtracting the elastic tail from the data is $\ll 1\%$, determined by considering different models for the elastic ^{3}He form factors.

In a similar fashion as the elastic tail, the systematic effect of the subtraction of the quasi-elastic tail was determined by considering different quasi-elastic cross section models to compute the tail. We found that the error is $\approx$ 5–6% for the lowest bin in E_p, and falling to $\approx$ 1% for all other bins for which we have data.

To determine the error related to the material thicknesses in the electron's path, we varied the thicknesses in our calculations by up to 10%, and saw a change in our resulting Born cross section of $\lesssim$ 1.5%.

The error corresponding to the input model used in the radiative correction prodecure was determined by using different models. The resulting Born cross section changed by at most $\approx$ 5% for the lowest bin in E_p and dropped to $\lesssim$ 1% for all other bins.

1.3.5 The Double-Spin Asymmetries

The BigBite spectrometer was used to measure the parallel and perpendicular double-spin asymmetries between longitudinally polarized electrons and a longitudinally or transversely polarized ^{3}He target. These asymmetries were then corrected for imperfect beam and target polarizations. Corrections were also made for dilution effects due to the presence of N_2 in the target [31], and contamination due to pions and pair-produced electrons. The full details of these analyses may be found in [34, 35].

1.3.6 Asymmetry Radiative Corrections

To compute the radiative corrections for asymmetries, we utilize the radiative correction code RADCOR mentioned in Section 1.3.3. To do this, we carry out the corrections on polarized cross section differences, $\Delta\sigma$, related to asymmetries by:

$$\Delta\sigma^r_{\parallel,\perp} = 2\sigma^r_0 A^r_{\parallel,\perp}, \tag{12}$$

where $A_{\parallel,\perp}$ indicates a radiated asymmetry where the target is polarized either parallel ($\parallel$) or perpendicular ($\perp$) with respect to the incident electron beam polarization. The unpolarized cross section is σ^r_0, where the r indicates that radiative effects have been added in. After the data have been converted to polarized cross section differences, they are imported into the RADCOR code in a similar fashion as was done for the unpolarized cross sections. The difference here, however, is that a model for the polarized cross section differences is needed to complete the integrals mentioned in Equation 11. This model consists of three components describing different types of physics:

- DIS,
- the quasi-elastic region,
- and the resonance region.

The model used for the DIS region was the DSSV global analysis parton distribution function (PDF) model [43], which describes world data quite well in our kinematic region of interest. For the quasi-elastic region, we utilized P. Bosted's nucleon form factors [44], smeared by a quasi-elastic scaling function [45] to simulate the nuclear effects of ^{3}He. Putting together the nucleon form factors and the smearing function yields a quasi-elastic $\Delta\sigma$ which fits world data well. For the resonance region, we used the MAID model [14], which also does well describing world data. Putting the DIS, quasi-elastic and resonance contributions together, we build up an appropriate $\Delta\sigma$ that describes the physics to a reasonable level, an example of which is shown in Figure 5 where we compare our model to JLab E94-010 data [11, 12]. In the radiative correction procedure, the quasi-elastic tail was not subtracted first, but rather included in the integration. The elastic tail was found to be very small and was not subtracted.

To minimize statistical flucuations in the radiative corrections, the corrections were done to a model of our data set. After obtaining the Born $\Delta\sigma$ from RADCOR, the corresponding asymmetry was obtained by inverting Equation 12 (but using the *Born* σ_0) to find A. Then, the size of the radiative correction at the asymmetry level was determined as:

$$\Delta A = A_b - A_r, \tag{13}$$

where A_b is the Born asymmetry and A_r is the radiated asymmetry. This ΔA was applied to our data for both the parallel and perpendicular cases as an additive correction. The size of the radiative correction as a function of x is shown in Figure 6. The gray band indicates the systematic error, which is discussed in Section 1.3.7.

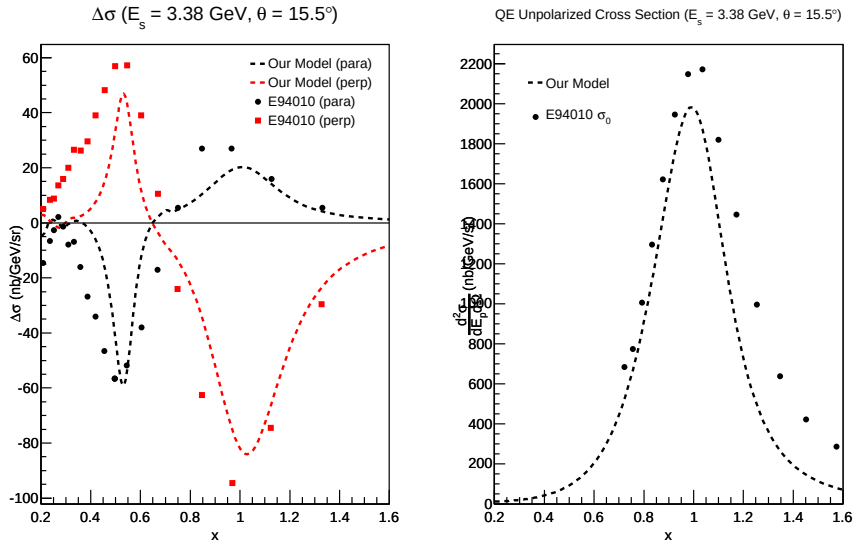

Figure 5: Our model of $\Delta\sigma_{\parallel,\perp}$ as compared to JLab E94-010 data. Our model consists of combining a smeared version of P. Bosted's nucleon form factors to describe the quasi-elastic region and the MAID model for the resonance region. The DIS region is modeled using the DSSV PDFs.

The Born asymmetries for our data and their systematic errors are shown in Figure 7. The error bars indicate the statistical errors, while the colored bands indicate the systematic errors, which were obtained by varying all of the inputs needed to extract the asymmetries within reasonable limits[1] and observing the change in the asymmetry.

1.3.7 Asymmetry Radiative Correction Systematic Errors

To investigate the systematic errors on the radiative corrections, there are two main contributions to consider: material thicknesses and model dependence.

To address the thicknesses, they were changed by $\pm$ 10% and the result was compared to the unmodified result. The change was found to be $\lesssim$ 1.5%, similar to what was seen for the unpolarized cross sections.

The model dependence of the radiative corrections was determined as follows: the input spectra to the integrals were varied *at random* by $\pm$ 10% for 30 trials, and the size of the correction changed by $\lesssim$ 5% where the change was seen to be the largest.

1.4 Preliminary Physics Results

1.4.1 The Virtual Photon-Nucleon Asymmetry

Figure 8 shows the preliminary results for $A_1^{^3\mathrm{He}}$ at E = 4.74 and 5.89 GeV, respectively. Also shown is world data from SLAC E142 [46] and JLab E01-012 [47] and E99-117 [20]. The red (blue) data points indicate our E = 4.74 GeV (E = 5.89 GeV) data. The error bars on the world data are the in quadrature sum of the statistical and systematic errors, while the error bars on our data are statistical only. The colored bands at the bottom of the plot indicate the systematic errors. The systematic errors were determined by varying all of the inputs to the computation of $A_1^{^3\mathrm{He}}$ to reasonable levels and observing the change in the asymmetry. The gray band represents various global analyses [21, 43, 50, 51, 52, 53, 54]. The data from this experiment are consistent with the world data across a wide range in x, despite the larger error bars in the resonance region, which corresponds to $x > 0.519\ (0.623)$ for E = 4.73 GeV (E = 5.89 GeV).

[1] Such quantities include the electron cuts, the nitrogen dilution factor, beam and target polarizations, and pion and pair production contamination factors.

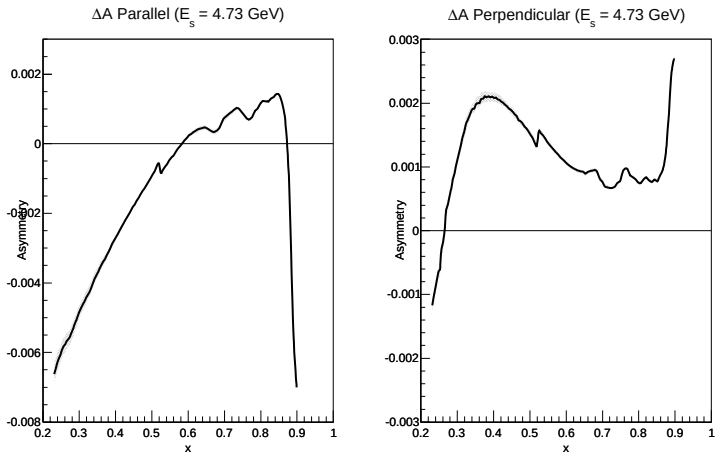

(a) E = 4.74 GeV

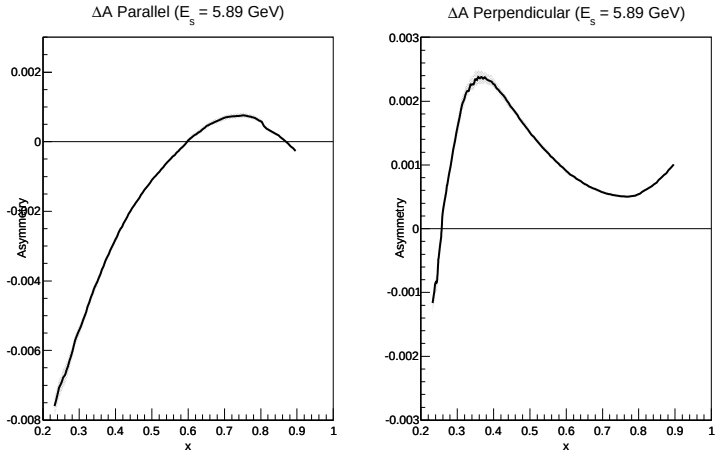

(b) E = 5.89 GeV

Figure 6: The size of the radiative correction on the asymmetries, defined as $\Delta A = A_b - A_r$. The gray band indicates the systematic error associated with the correction, see Section 1.3.7. The ΔA shown in these plots are applied to the data as an additive correction to obtain the Born asymmetry. (a): E = 4.74 GeV data; (b): E = 5.89 GeV data.

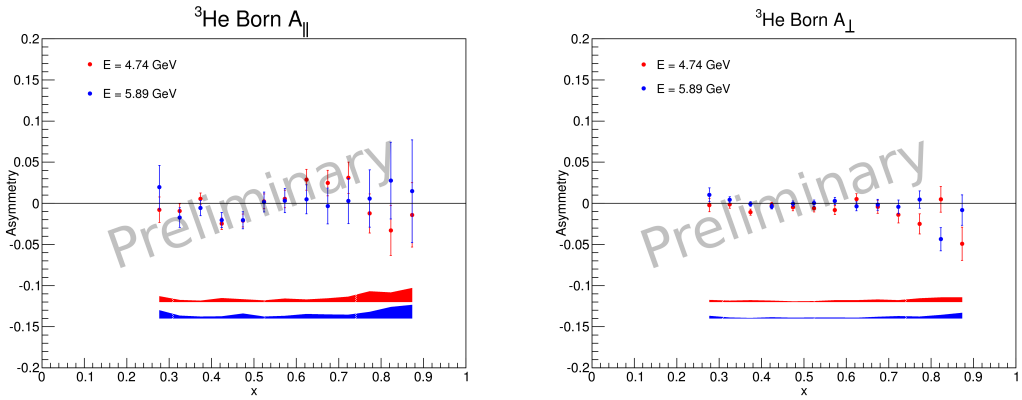

(a) Parallel Asymmetries

(b) Perpendicular Asymmetries

Figure 7: The Born asymmetries for E = 4.74 GeV (red) and E = 5.89 GeV (blue). The error bars indicate the statistical errors, while the colored bands show the systematic errors. (a): parallel asymmetries; (b): perpendicular asymmetries.

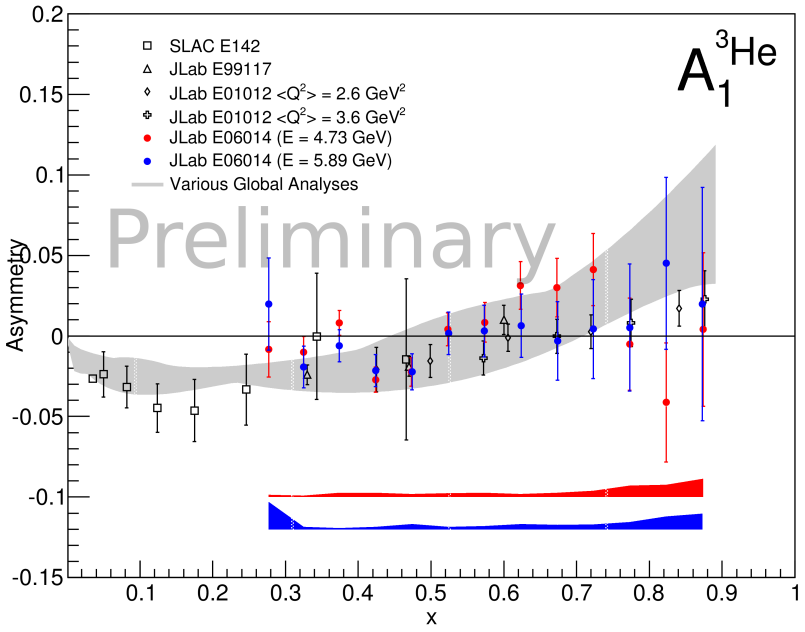

Figure 8: $A_1^{^3He}$ compared to the world data from SLAC E142 [46] and JLab E01-012 [47] and E99-117 [20]. The error bars on the world data indicate the in quadrature sum of statistical and systematic errors, while the error bars on our data are statistical only. The colored bands at the bottom of the plot show the systematic errors. The gray band shows an envelope of various global analyses [21, 43, 50, 51, 52, 53, 54].

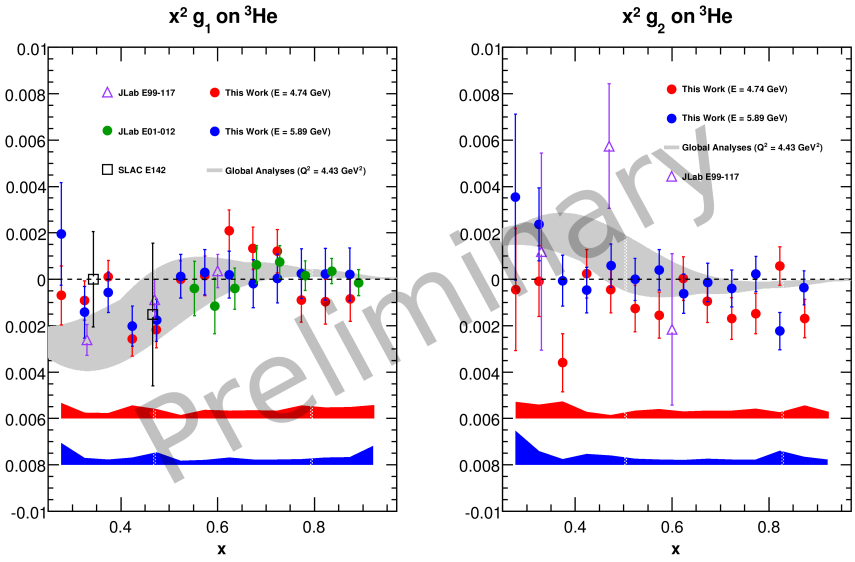

Figure 9: Preliminary results for the spin structure functions g_1 and g_2 on a ^{3}He target for E = 4.74 GeV (red) and 5.89 GeV (blue) compared to the world data [46, 47, 20] and various global analyses [21, 43, 50, 51, 52] represented by the gray band. The error bars on our data are statistical only; the colored bands at the bottom of the plot indicate the systematic errors.

1.4.2 The Spin Structure Functions

En route to extracting d_2^n, the spin structure functions g_1 and g_2 can be obtained according to:

$$g_1 = \frac{MQ^2}{4\alpha^2}\frac{2y}{(1-y)(2-y)}\sigma_0\left[A_\parallel + \tan(\theta/2)A_\perp\right] \quad (14)$$

$$g_2 = \frac{MQ^2}{4\alpha^2}\frac{y^2}{(1-y)(2-y)}\sigma_0\left[-A_\parallel + \frac{1+(1-y)\cos\theta}{(1-y)\sin\theta}A_\perp\right], \quad (15)$$

The preliminary results for $g_1{}^{^3\mathrm{He}}$ and $g_2{}^{^3\mathrm{He}}$ are shown in Figure 9, which compares the data to various models represented by the gray band [21, 43, 50, 51, 52] and the world data. The systematic errors on our data were obtained by varying all of the inputs needed to compute g_1 and g_2 to reasonable levels and observing the change in the result.

1.5 Current and Future Work

At present, we are working on finalizing our analysis to evaluate d_2^n and A_1^n. Additionally, from d_2^n we can extract the color electric and magnetic forces [3, 4, 5]. From our A_1^n data, we can also perform a flavor decomposition to obtain the quantities $\Delta u/u$ and $\Delta d/d$.

References

[1] S. Wandzura and F. Wilczek, Phys. Lett. B **72**, 2 (1977).

[2] R.L. Jaffe, Comm. Nucl. Part. Phys. **19**, 239 (1990).

[3] B.W. Filippone and Xiandong Ji, Adv. Nucl. Phys. **26**, 1 (2001). arXiv:0101224v1 [hep-ph].

[4] M. Burkardt, *The g_2 Spin Structure Function* (2009), arXiv:0905.4079v1 [hep-ph].

[5] M. Burkardt, *Parton Distributions in the Impact Parameter Space* (2008), arXiv:0902.0163v1 [hep-ph].

[6] S. Choi, X. Jiang, Z.-E. Meziani, B. Sawatzky *et al.*, Jefferson Lab PAC E06-014 (2005).

[7] M. Gockeler *et al.*, Phys. Rev. D **72**, 054507 (2005).

[8] P. Solvignon, private communication.

[9] E. V. Shuryak and A.I. Vainshtein, Nucl. Phys. B **201**, 141 (1982).

[10] Ji and Chou, Phys. Rev. D **42**, 3637 (1990).

[11] M. Amerian *et al.*, Phys. Rev. Lett. **89**, 242301 (2002).

[12] K. Slifer *et al.*, Phys. Rev. Lett. **101**, 022303 (2008)

[13] K. Slifer *et al.*, *Resonance Spin Structure*, 2008. arXiv:0812.0031.

[14] D. Drechel, S.S. Kamolov and L. Tiatar, Eur. Phys. J. **A34**, 69 (2007).

[15] P.L. Anthony *et al.*, Phys. Lett. B **553**, 18 (2003).

[16] N. Isgur, Phys. Rev. D **59**, 0340123 (1999).

[17] K. Abe *et al.*, SLAC-PUB-7753 (Feb. 1998).

[18] K. Abe *et al.*, Phys. Rev. Lett. **79**, 26 (1997); Phys. Lett. B **405**, 180 (1997).

[19] K. Ackerstaff *et al.*, Phys. Lett. B **404**, 383 (1997).

[20] X. Zheng *et al.*, Phys. Rev. C **70**, 065207 (2004).

[21] E. Leader, A.V. Siderov, D.B. Stamenov, Int. J. Mod. Phys **A13**, 5573 (1998).

[22] H. Avakian, S. Brodsky and A. Deur *et al.*, Phys. Rev. Lett. **99**, 082001 (2007).

[23] J.P. Ralson, P. Jain, R.V. Buniy, AIP Conf. Proc. **549**, 302 (2000).

[24] K.V. Dharmawardane *et al.*, Phys. Lett. B **641**, 11 (2006).

[25] G. Cates, N. Liyanage, Z.-E. Meziani, G. Rosner, B. Wojtsekhowski, X. Zheng *et al.*, Jefferson Lab PAC E1206122 (2006).

[26] G. Cates, J.P. Chen, Z.-E. Meziani, X. Zheng *et al.*, Jefferson Lab PAC E1210101 (2010).

[27] J.L. Friar *et al.*,Phys. Rev. C **42**, 6 (1990).

[28] F. Bissey, A.W. Thomas and I.R. Afnan, Phys. Rev. C **64**, 024004 (2001).

[29] M. Anselmino *et al.*, Phys. Rep. **261**, 1–124 (1995).

[30] D. Parno, Ph.D. Thesis, Carnegie Mellon University (2011).

[31] I. Kominis, Ph.D. Thesis, Princeton University (2001).

[32] J. Singh, *A Note About Beam Depolarization*, Univeristy of Virginia (2008).

[33] D. Parno *et al.*, E06-014 Analysis Status Report 2010, https://hallaweb.jlab.org/wiki/images/b/b3/D2n_Annual_Report_2010.pdf

[34] M. Posik *et al.*, E06-014 Analysis Status Report 2011, https://hallaweb.jlab.org/wiki/images/8/8c/D2n_HallAReport_2011_v5.pdf

[35] D. Flay *et al.*, E06-014 Analysis Status Report 2012, https://hallaweb.jlab.org/wiki/images/7/7a/E06014-2012.pdf

[36] L.W. Mo and Y.S. Tsai, Rev. Mod. Phys. **40**, 205 (1969).

[37] R. Altulmus and J. Wise, rosetail.f, fortran analysis code.

[38] Amroun *et al.*, Nucl. Phys. A **579**, 596 (1994).

[39] J. W. Lightbody and J. S. O'Connell, Comp. in Phys., 57 (1988).

[40] S. Stein *et al.*, Phys. Rev. D **12**, 1884 (1975).

[41] Roy Whitney, radcor.f, fortran analysis code.

[42] P.E. Bosted and V. Mamyan, *Empirical Fit to electron-nucleus scattering* (2012), arXiv:1203.2262v2 [nucl-th].

[43] D. de Florian, R. Sassot, M. Stratmann and W. Vogelsang, Phys. Rev. Lett. **101**, 072001 (2008).

[44] P.E. Bosted, Phys. Rev. C **51**, 409 (1995).

[45] J. E. Amaro, M. B. Barbaro, J. A. Caballero, T. W. Donnelly, A. Molinari and I. Sick, Phys. Rev. C **71**, 015501 (2005).

[46] P.L. Anthony *et al.*, Phys. Rev. D **54**, 6620 (1996).

[47] P. Solvignon *et al.*, Phys. Rev. Lett. **101**, 182502 (2008).

[48] F. Bissey *et al.*, Phys. Rev. C **65**, 064317 (2002).

[49] S.A. Kulagin and W. Melnitchouk, Phys. Rev. C **78**, 065203 (2008).

[50] H. Weigel, L. Gamberg and H. Reinhart, Phys. Rev. D **55**, 6910 (1997).

[51] C.R.V. Bourrely, J. Soffer and F. Buccella, Eur. Phys. J. C **41**, 327 (2005) [arXiv:hep-ph/0502180].

[52] M. Stratmann, Z. Phys. C **60**, 763 (1993).

[53] J. F. Owens, A. Accardi and W. Melnitchouk, Phys. Rev. D **87**, 094012 (2013).

[54] J. Pumplin, D. R. Stump and J. Huston *et al.*, J. High Energy Phys. **7**, 012 (2002).